Bridged Polystannoxane: A New Route toward Nanoporous Tin Dioxide

Thierry Toupance,*,† Hicham El Hamzaoui,† Bernard Jousseaume,† Hocine Riague,† Iyad Saadeddin,‡ Guy Campet,‡ and Joachim Brötz§

Laboratoire de Chimie Organique et Organométallique, UMR 5802 CNRS, Université Bordeaux 1, 351 Cours de la Libération, F-33405 Talence Cedex, France, Institut de Chimie de la Matière Condensée de Bordeaux, UPR 9048 CNRS, Château Brivazac, Avenue du Docteur A. Schweitzer, F-33608 Pessac Cedex, France, and Institute of Material Science, Darmstadt University of Technology, Petersenstrasse 23, D-64287 Darmstadt, Germany.

Received August 21, 2006. Revised Manuscript Received October 23, 2006

Hydrolysis and condensation under acidic conditions of bis(triprop-1-ynylstannyl)*p*-phenylene **1**, *p*-xylene **2**, or butylene **3** precursors yielded bridged polystannoxanes in the form of xerogels after being dried under reduced pressure. The gels were amorphous and nonporous with very low specific surface areas. Thermal treatment of the xerogels in air at 400−500 °C resulted in nanocrystalline nanoporous cassiterite tin dioxide materials, which have been thoroughly characterized by elemental analysis, FTIR, TGA−MS, powder XRD, and N_2 adsorption porosimetry. The calcined materials consisted of a porous network of aggregated nanoparticles with a nanoporosity stemming from the interparticle space. A careful tuning of the precursor nature and the calcination conditions enabled the synthesis of materials with Brunauer−Emmet−Teller surface areas ranging from 40 to 150 $m^2\ g^{-1}$, a mean pore size between 3.5 and 12 nm, and an average particle size of 5 to 25 nm. Starting from precursor **1** appeared to be the best strategy to obtain pure nanocrystalline tin dioxide materials with good textural properties for applications, with the *p*-phenylene bridge being easily removed by calcination.

Introduction

Fabrication of nanostructured nanoporous semiconductors has attracted worldwide attention, stimulated by their outstanding chemical, electronic, magnetic, and optical properties and their use as nanoscale devices, combined with the ever ongoing miniaturization efforts. Among the binary and ternary oxides available, tetragonal tin dioxide (with a rutile-like structure), SnO_2 is one of the most important smart and functional materials for technological and industrial applications because of its unique chemical and mechanical stabilities and two specific characteristics: variation in valence state and oxygen vacancies. Furthermore, its electronic conductivity can be easily enhanced by doping with fluorine or antimony.[1] This wide band gap semiconductor has therefore been used extensively for applications such as transparent conductive electrodes for optoelectronic devices,[2] electrochromic displays,[3] solar energy conversion,[4] heat mirrors,[5] photocatalysis,[6] and anode materials for lithium-ion batteries.[7] Furthermore, as an n-type semiconductor, tin dioxide is extremely sensitive to reducing gas as CO,[8] H_2,[9] nitrogen oxides,[10] or ethanol[11] and, also, to harmful gas such as HF.[12] Tin dioxide is therefore commonly employed as an active layer in gas sensors.

Most of these applications require the synthesis of nanocrystalline tin dioxide materials with well-defined particle size distributions and large specific surface areas. Indeed, it is noteworthy that both the conductivity and sensitivity of SnO_2-based gas sensors are governed by the grain size,[13] whereas an optimal SnO_2 nanoparticle size has been found

* Corresponding author. E-mail: t.toupance@lcoo.u-bordeaux1.fr.
† Université Bordeaux 1.
‡ CNRS.
§ Darmstadt University of Technology.

(1) Gordon, R. G. *MRS Bull.* **2000**, *25*, 52.
(2) Chopra, K. L.; Major, S.; Pandya, D. K. *Thin Solid Films* **1983**, *102*, 1.
(3) Cummins, D.; Boschloo, G.; Ryan, M.; Corr, D.; Rao, S. N.; Fitzmaurice, D. *J. Phys. Chem. B* **2000**, *104*, 11449.
(4) (a) Ferrere, S.; Zaban, A.; Gregg, B. A. *J. Phys. Chem. B* **1997**, *101*, 4490. (b) Srivastava, D. N.; Chappel, S.; Palchik, O.; Zaban, A.; Gedanken, A. *Langmuir* **2002**, *18*, 4160. (c) Kay, A.; Grätzel, M. *Chem. Mater.* **2002**, *14*, 2930.
(5) (a) de Waal, H.; Simonis, F. *Thin Solid Films* **1981**, *77*, 253. (b) Manifacier, J. C. *Thin Solid Films* **1982**, *90*, 297.
(6) (a) Miyauchi, M.; Nakajima, A.; Watanabe, T.; Hashimoto, K. *Chem. Mater.* **2002**, *14*, 2812. (b) Cun, W.; Jincai, Z.; Xinming W.; Bixian, M.; Guoying, S.; Ping'an, P.; Jiamo, F. *Appl. Catal., B.* **2002**, *39*, 269.
(7) (a) Itoda, Y.; Kubota, T.; Matsufuji, A.; Maekawa, Y.; Miyasaka, T. *Science* **1997**, *276*, 1395. (b) Zhu, J.; Lu, Z.; Aruna, S. T.; Aurbach, D.; Gedanken, A. *Chem. Mater.* **2000**, *12*, 2557. (c) Wang, Y.; Lee, J. Y. *J. Phys. Chem.* **2004**, *108*, 17832. (d) Wang, Y.; Lee, J. Y. *J. Power Sources* **2005**, *144*, 220. (e) Ha, H. W.; Kim, K.; de Borniol, M.; Toupance, T. *J. Solid State Chem.* **2006**, *179*, 689.
(8) (a) Harrison, P. G. *Nature* **1988**, *332*, 337. (b) Wang, Z. L. *Adv. Mater.* **2003**, *15*, 432. (c) Kolmakov, A.; Zhang, Y.; Cheng, G.; Moskovits, M. *Adv. Mater.* **2003**, *15*, 997.
(9) (a) Tournier, G.; Pijolat, C. *Sens. Actuators, B* **2005**, *100*, 553. b) Han, C. H.; Han, S. D.; Singh, I.; Toupance, T. *Sens. Actuators, B* **2005**, *109*, 264.
(10) a) Leblanc, E.; Perier-Camby, L.; Thomas, G.; Gibert, R.; Primet, M.; Gelin, P. *Sens. Actuators, B 2000*, *62*, 67. (b) Hyodo, T.; Sasahara, K.; Shimizu, Y.; Egashira, M. *Sens. Actuators, B* **2005**, *106*, 580.
(11) (a) Brousse, T.; Beutier, D.; Schleich, D. M. *Ionics* **1995**, *1*, 499. (b) Leite, E. R.; Weber, I. T.; Longo, E.; Varela, J. A. *Adv. Mater.* **2000**, *12*, 965.
(12) (a) Sanchez, J. B.; Berger, F.; Fromm, M.; Nadal, M. H. *Sens. Actuators, B* **2005**, *106*, 826. (b) Sanchez, J. B.; Berger, F.; Daniau, W.; Blind, P.; Fromm, M.; Nadal, M. H. *Sens. Actuators, B* **2006**, *113*, 1017.

10.1021/cm061964d CCC: $33.50
Published on Web 12/05/2006

for the use of nanocrystalline tin dioxide in dye-sensitized solar cells.[14] In this context, many routes have been explored for preparing tin dioxide materials of various shapes and morphologies, including oxidation[15] or evaporation[16] under stringent conditions, hydrothermal,[17] pyrolysis of organotins[18] or electrochemical deposition[19] followed by thermal oxidation, and hydrolytic[20] and non-hydrolytic[21] sol−gel and sonochemical methods.[22] Tin dioxide nanobelts,[15] nanotubes,[16] nanorods,[17] nanowires,[19] and spherical nanoparticles[18,20,21] were thus obtained. In addition, the development of synthetic strategies providing materials with well-defined porosity is a key step toward efficient gas sensors or solar cells, as it should make the diffusion of gaseous species or electrolytes into the porous materials easier.

Over the past decade, the "template" or "organic surfactant" approach has led to a wide range of metal oxides exhibiting well-defined morphology and porosity. First reported for silica,[23] this was generalized to block copolymers[24] and transition metal oxides[25] and more recently extended to the preparation of thin films.[26] Nonetheless, only a few examples of mesoporous tin dioxide have been reported according to this route, but it turned out that the obtained structures were unstable after removal of the surfactant and thermal treatment above 350 °C.[27] Aside from the template route, an original two-step procedure has been developed for mesoporous silica-based materials. The first step consists of the preparation of bridged silsesquioxane hybrid materials resulting from the hydrolysis and condensation of bis(trialkoxysilyl)alkylene, arylene, or benzylene derivatives with[28] or without[29] a surfactant. The organic spacer is then removed by air oxidation at high-temperature preceded or not by a chemical treatment to yield mesoporous silicas.[30] However, this neat approach has not been extended to other metal oxides so far, probably because of the lack of accessible precursors. As tin is one of the rare metal atoms that forms stable metal−carbon bonds under hydrolytic conditions, we set out new synthetic strategies for the preparation of hydrolyzable organotins for sol−gel chemistry purposes.[31] Thus, we have described the synthesis of alkylene-, arylene-, and benzylene-bridged ditin hexaalkynides[32] which led to self-assembled tin-based hybrid materials under certain hydrolytic conditions.[33]

Scheme 1. Bis(triprop-1-ynylstannyl)alkyl and -aryl Derivatives Used as Sol−Gel Precursors in This Study

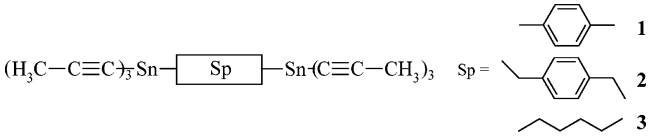

In this paper, we report on nanoporous cassiterite tin dioxide materials that were prepared from bridged-polystannoxane obtained by hydrolysis of bis(triprop-1-ynylstannyl)*p*-phenylene **1**, *p*-xylene **2**, or butylene **3** monomers (Scheme 1). The study deals with the control of both the morphology and texture of the powders prepared by varying the nature of the organic spacer and tuning the hydrolysis conditions and temperature of the thermal treatment employed to crystallize the materials. Nanocrystalline nanoporous tin dioxide materials stable to 400−500 °C with specific surface areas as high as 110 $m^2\ g^{-1}$ were produced.

Experimental Section

Materials. Dry solvents (THF, hexanes) were distilled over Na/benzophenone prior to use. Elemental analyses were performed by

(13) Xu, C.; Tamaki, J.; Miura, N.; Yamazoe, N. *Sens. Actuators, B* **1991**, *3*, 147.
(14) Chappel, S.; Zaban, A. *Sol. Energy Mater. Sol. Cells* **2002**, *71*, 141.
(15) Duan, J.; Yang, S.; Liu, H.; Gong, J.; Huang, H.; Zhao, X.; Zhang, R.; Du, Y. *J. Am. Chem. Soc.* **2005**, *127*, 6180.
(16) (a) Dai, Z. R.; Pan, Z. W.; Wang, Z. L. *J. Am. Chem. Soc.* **2002**, *124*, 8673. (b) Dai, Z. R.; Gole, J. L.; Stout, J. D.; Wang, Z. L. *J. Phys. Chem. B* **2002**, *106*, 1274.
(17) Zhang, D. F.; Sun, L. D.; Yin, J. L.; Yan, C. H. *Adv. Mater.* **2003**, *15*, 1022.
(18) (a) Nayral, C.; Ould-Ely, T.; Maisonnat, A.; Chaudret, B.; Fau, P.; Lescouzères, L.; Peyre- Lavigne, A. *Adv. Mater.* **1999**, *11*, 61. (b) Nayral, C.; Viala, E.; Fau, P.; Senocq, F.; Jumas, J-C.; Maisonnat, A.; Chaudret, B. *Chem. Eur. J.* **2000**, *6*, 4082. (c) Nayral, C.; Viala, E., Collière, V.; Fau, P.; Senocq, F.; Maisonnat, A.; Chaudret, B. *Appl. Surf. Sci.* **2000**, *164*, 219.
(19) Zheng, M.; Li, G.; Zhang, X.; Huang, S.; Lei,Y.; Zhang, L. *Chem. Mater.* **2001**, *13*, 3859.
(20) (a) de Monredon, S.; Cellot, A.; Ribot, F.; Sanchez, C.; Armelao, L.; Gueneau, L.; Delattre, L. *J. Mater. Chem.* **2002**, *12*, 2396. (b) Broussous, L.; Santilli, C. V.; Pulcinelli, S. H.; Craievich, A. F. *J. Phys. Chem. B* **2002**, *106*, 2855. (c) Toupance, T.; Babot, O.; Jousseaume, B.; Vilaça, G. *Chem. Mater.* **2003**, *15*, 4691. (d) Briois, V.; Belin, S.; Zucolotto Chalaça, M.; Santos, R. H. A.; Santilli, C. V.; Pulcinelli, S. H. *Chem. Mater.* **2004**, *16*, 3885.
(21) Pinna, N.; Neri, G.; Antonietti, M.; Niederberger, M. *Angew. Chem., Int. Ed.* **2004**, *43*, 2.
(22) Pang, G.; Chen, S.; Koltypin, Y.; Zaban, A.; Feng, S.; Gedanken, A. *Nano Lett.* **2001**, *12*, 723.
(23) (a) Kresge, C. T.; Leconowicz, M. E.; Roth, W. J.; Vartuli, J. C.; Beck, J. S. *Nature* **1992**, *359*, 710. (b) Beck, J. S.; Vartuli, J. C.; Roth, W. J.; Leonowicz, M. E.; Kresge, C. T.; Schmitt, K. D.; Chu, C. T. W.; Olson, D. H.; Sheppard, E. W.; Mc Cullen, S. B.; Higgins, J. B.; Schlenker, J. L. *J. Am. Chem. Soc.* **1992**, *114*, 10834.
(24) Zhao, D.; Huo, Q.; Feng, J.; Chmelka, B. F.; Stucky, G. D. *J. Am. Chem. Soc.* **1998**, *120*, 6024.
(25) (a) Yang, P.; Zhao, D.; Margolese, I.; Chmelka, B. F.; Stucky, G. D. *Chem. Mater.* **1999**, *11*, 2813. (b) Galarneau, A.; Cambon, H.; Di Renzo, F.; Fajula, F. *Langmuir* **2001**, *17*, 83128.
(26) (a) Grosso, D.; Soler-Illia, G. J. de A. A.; Crepaldi, E. L.; Cagnol, F.; Sinturel, C.; Bourgeois, A.; Brunet-Bruneau, A.; Amenitsch, H.; Albouy, P. A.; Sanchez, C. *Chem. Mater.* **2003**, *15*, 4562. (b) Smarsly, B.; Grosso, D.; Brezesinski, T.; Pinna, N.; Boissière, C.; Antonietti, M.; Sanchez, C. *Chem. Mater.* **2004**, *16*, 2948. (c) Brezesinski, T.; Erpen, C.; Iimura, K.-I.; Smarsly, B. *Chem. Mater.* **2005**, *17*, 1683.
(27) (a) Abdel-Fattah, T. M.; Pinnavaia, T. J. *J. Chem. Soc., Chem. Commun.* **1996**, 665. (b) Severin, K. G.; Abdel-Fattah, T. M.; Pinnavaia, T. J. *J. Chem. Soc., Chem. Commun.* **1998**, 1471. (c) Ulagappan, N.; Rao, C. N. R. *J. Chem. Soc., Chem. Commun.* **1996**, 1685. (d) Qi, L.; Ma, J.; Cheng, M.; Zhao, Z. *Langmuir* **1998**, *14*. 1685. (e) Chen, F.; Liu, M. *Chem. Commun.* **1999**, 1829.
(28) (a) Inagaki, S.; Guan, S.; Fukushima, Y.; Ohsuna, T.; Terasaki, O. *J. Am. Chem. Soc.* **1999**, *121*, 9611. (b) Melde, B. J.; Hollande, B.; Blanford, C. F.; Stein, A. *Chem. Mater.* **1999**, *11*, 3302. (c) Asefa, T.; MacLachlan, M. J.; Coombs, N.; Ozin, G. A. *Nature* **1999**, *402*, 867. (d) Hunks, W. J.; Ozin, G. A. *Chem. Mater.* **2004**, *16*, 5465.
(29) (a) Shea, K. J.; Loy, D. A.; Webster, O. *J. Am. Chem. Soc.* **1992**, *114*, 6700. (b) Loy, D. A.; Shea, K. J. *Chem. Rev.* **1995**, *95*, 1413. (c) Hobson, S. T.; Shea, K. J. *Chem. Mater.* **1997**, *9*, 616. (d) Corriu, R. J. P.; Moreau, J. J. E.; Thepot, P.; Wong Chi Man, P. *Chem. Mater.* **1992**, *4*, 1217. (e) Ben, B.; Boury, B.; Corriu, R. J. P.; Le Strat, V. *Chem. Mater.* **2000**, *12*, 3249. (f) Boury, B. Corriu, R. J. P. *Chem. Rec.* **2003**, *3*, 120.
(30) Corriu, R. *Polyhedron* **1998**, *17*, 925.
(31) (a) Jousseaume, B.; Lahcini, M.; Rascle, M. C.; Ribot, F.; Sanchez, C. *Organometallics* **1995**, *14*, 685. (b) Jaumier, P.; Jousseaume, B.; Lahcini, M.; Ribot, F.; Sanchez, C. *Chem. Commun.* **1998**, 369. (c) Jaumier, P.; Lahcini, M.; Jousseaume, B. *Angew. Chem., Int. Ed.* **1999**, *36*, 402.
(32) Jousseaume, B.; Riague, H.; Toupance, T.; Lahcini, M.; Mountford, P.; Tyrrell, B. R. *Organometallics* **2002**, *21*, 4590.
(33) (a) El Hamzaoui, H.; Jousseaume, B.; Riague, H.; Toupance, T.; Dieudonné, P.; Zakri, C.; Maugey, M.; Allouchi, H. *J. Am. Chem. Soc.* **2004**, *126*, 8130. (b) El Hamzaoui, H.; Jousseaume, B.; Toupance, T.; Zakri, C.; Biesemans, M.; Willem, R.; Allouchi, H. *Chem. Commun.* **2006**, 1304.

the "Service Central d'Analyze du CNRS" in Vernaison, France. 1,4-Bis(triprop-1-ynylstannyl)benzene **1**, 1,4-bis(triprop-1-ynylstannylmethyl)benzene **2**, and 1,4-bis(triprop-1-ynylstannyl)butane **3** were synthesized as previously described.[32]

Preparation of the Xerogels. At room temperature, a mixture of water and THF containing a catalytic amount of hydrochloric acid was added to a stirred solution of precursor **1**−**3** in THF. Approximately 38 equiv. of water per tin center were introduced, and the molar ratio between the precursor and THF was maintained at around 130:1. After being stirred for 10 min, the mixtures were stood for at room temperature. The gel transitions were well-defined, with the solution becoming viscous and then "freezing" into a gel over a span of a dozen hours. Once gelation occurred, the gels were allowed to cure at room temperature for 8 days. The solvent was then removed under reduced pressure, and the resulting solids were washed with THF (3 × 10 mL) to remove undesirable organics. The powders were finally dried in vacuo at 120 °C for 3 h to yield white xerogels. In the following, the samples are labeled G_p^T, where p and T stand for the precursor label and the temperature of the thermal treatment, respectively.

(G_1^{120}): **1** 2 g, 3.65 mmol; H_2O 5 mL, 277 mmol; 1 M HCl 0.5 mL, 0.5 mmol; THF 38 mL. After drying, a yield of about 1.2−1.3 g was typically recovered. Elemental anal. Calcd for $Sn_2(C_6H_4)O_{2.5}(OH)_1(THF)_{0.2}\cdot 1.2H_2O$ (wt %): Sn, 58.4; O, 19.3; C, 20.1; H, 2.2. Found: Sn, 58.5; O, 19.5; C, 19.9; H, 2.0.

(G_2^{120}) 2 1.24 g, 2.15 mmol; H_2O 2.94 mL, 163.3 mmol; 1 M HCl 0.294 mL, 0.294 mmol; THF 22.7 mL. After drying, a yield of about 0.8−0.85 g was typically recovered. Elemental anal. Calcd for $Sn_2(CH_2-C_6H_4-CH_2)O_{2.8}(OH)_{0.4}(THF)_{0.4}\cdot H_2O$ (wt %): Sn, 53.9; O, 16.7; C, 26.2; H, 3.1. Found: Sn, 52.9; O, 17.1; C, 26.4; H, 2.6.

(G_3^{120}) 3 2 g, 3.8 mmol; H_2O 5.2 mL, 288 mmol; 1 M HCl 0.52 mL, 0.38 mmol; THF 40 mL. After drying, a yield of about 1.2−1.3 g was typically recovered. Elemental anal. Calcd for $Sn_2(CH_2)_4O_{2.9}(OH)_{0.2}(THF)_{0.2}\cdot 0.2H_2O$ (wt %): Sn, 65.7; O, 15.5; C, 15.9; H, 2.8. Found: Sn, 65.1; O, 14.9; C, 15.5; H, 2.7.

Pyrolysis experiments were conducted by treating the hybrid xerogels in an oxygen flow for 4 h at 400 or 500 °C. The chemical composition of the resulting powders was determined by elemental analysis. G_1^{400} (exp, wt %): Sn, 75.1; O, 24.0; C, 0.3. G_1^{500} (exp, wt %): Sn, 75.3; O, 20.5; C, 0.3. G_2^{400} (exp; wt %): Sn, 76.5; O, 20.8; C, 2.7. G_2^{500} (exp, wt %): Sn, 78.0; O, 21.8; C, 0.2. G_3^{400} (exp, wt %): Sn, 78.5; O, 19.7; C, 1.8. G_3^{500} (exp, wt %): Sn, 74.6; O, 24.9; C, 0.5.

Sample Characterization. Solution ^{1}H NMR spectra were recorded on a Bruker AC-250 spectrometer using d_8-THF as the solvent. Infrared spectra (KBr pellets) were obtained in the absorption mode using a FTIR Perkin-Elmer spectrophotometer. TGA−MS studies were carried out on a Netzsch STA simultaneous analyzer coupled with a Thermostar Balzers Instruments quadrupole spectrometer. Thermogravimetry (TG) traces were recorded in the 50−600 °C temperature range with a heating rate of 10 °C min^{-1} under an air or nitrogen flow. Powder X-ray diffraction patterns were collected on a Philips θ-2θ PW1820 diffractometer. A continuous scan mode was used to collect 2θ data from 5 to 60° with a 0.1 sampling pitch and a 2° min^{-1} scan rate. TEM micrographs were obtained using a JEOL-JEM 100 SX microscope. The samples were prepared by a pickup from a suspension of dried or calcined powder in acetone or methanol.

The texture of the dried and calcined samples was analyzed by nitrogen adsorption isotherm (77 K) measurements. Data collection was performed by the static volumetric method, using an ASAP2010 (Micromeritics) apparatus. Prior to each measurement, the samples were degassed at 120 °C in vacuo for a time interval high enough to reach a constant pressure (<10 μmHg). The BET equation was applied between 0.05 and 0.3 relative pressures to provide specific surface areas. Total pore volumes were determined by the amount of nitrogen adsorbed at a 0.99 relative pressure. Pore size distributions were evaluated by the Barrett, Joyner, Halenda (BJH) method for mesopores (pores of diameter 2−50 nm).[34] The adsorption isotherm was used to determine the overall pore size distribution, and the calculation was performed by the Micromeritics software package, which uses the recurrent method and applies the Harkins and Jura equation for the multilayer thickness. Nonetheless, in some cases, closure of the hysteresis loop at $P/P_0 = 0.42$ revealed the presence of very small pores. As a result, density functional theory (DFT) calculations were also performed to determine small pore sizes.

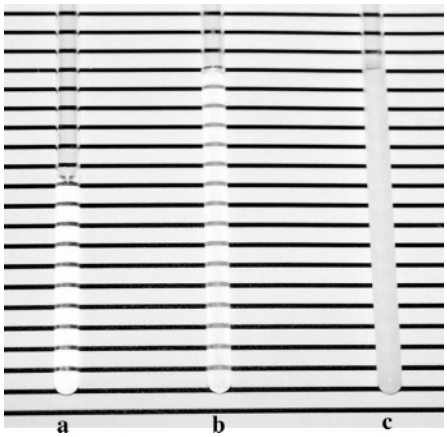

Figure 1. Hydrolytic behavior of **1** in THF: (a) starting solution; (b) after hydrolyis under acidic conditions [H_2O]/[Sn] = 38, [HCl]/{Sn} = 0.05; (c) after hydrolysis under basic conditions [H_2O]/[Sn] = 38, [NaOH]/{Sn} = 0.05.

Results

Hydrolytic Behavior and Characterization of the Xerogels. The gels were synthesized by hydrolysis and polycondensation of precursors **1**−**3**. Preliminary studies have shown that gelling of neutral solutions of **1** required several days.[35] Acidic or basic conditions were therefore necessary to quicken the process. Regardless of the precursor nature and the amount of water used, a mixture of gel and precipitate was systematically obtained upon base-catalyzed hydrolysis. In contrast, acid-catalyzed hydrolyzes led to transparent gels within several hours when a very large excess of water was employed (Figure 1). In this case, the gels remained transparent after aging at room temperature for more than one week. In the following, we therefore focus on the characterization of the samples prepared under acidic conditions.

First of all, the cleavage of the tin−propynyl bond during the hydrolysis of **1** was followed by ^{1}H NMR spectroscopy. As expected, the singlet at 2.2 ppm, with its sets of $^{117/119}$Sn satellites assigned to the methyl protons of the prop-1-ynyl groups, decreased progressively as the gelling proceeded, with the concomitant increase in the resonances at 2.1 (doublet) and 2.4 (quartet) ppm, characteristic of the propyne released. After 5 days, only the resonances of the propyne

(34) (a) Barrett, E. P.; Joyner, L.; Halenda, P. P. *J. Am. Chem. Soc.* **1951**, *73*, 373. (b) Olivier, J. P. *J. Porous Mater.* **1995**, *2*, 9.
(35) Jousseaume, B.; Riague, H.; Toupance, T.; Lahcini, M. In *Organic/Inorganic Hybrid Materials*; Laine, R., Sanchez, C., Giannelis, E., Eds.; Materials Research Society: Pittsburgh, PA, 2002; Vol. 726, p 105.

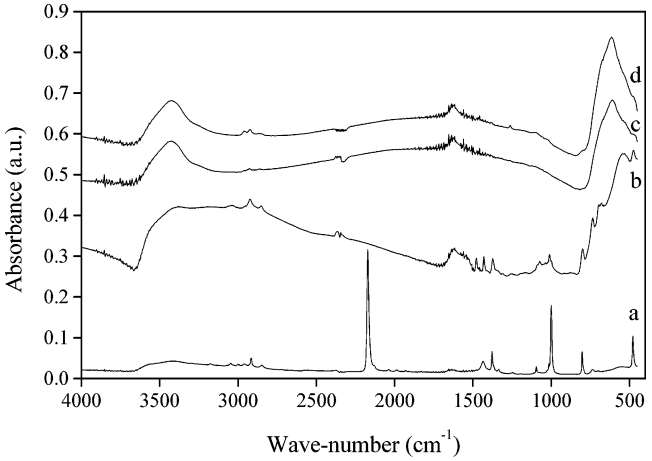

Figure 2. Infrared spectra of (a) **1**, (b) G_1^{120}, (c) G_1^{400}, and (d) G_1^{500}.

remaining trapped in the gel were detected. However, the departure of all prop-1-ynyl groups could not be definitely concluded on the basis of the ^{1}H NMR results because the hydrolysis−condensation process gave rise to oxo-polymeric species that might be silent in "solution" ^{1}H NMR because of their longer reorientation times. To have a better insight into the completion of the hydrolysis reaction, we also studied the xerogels obtained after drying by FTIR spectroscopy. The FTIR spectra of **1** and G_1^{120} are depicted in Figure 2. The disappearance of the typical bands of the Sn−C≡C group (2172 and 1000 cm^{-1}) in the IR spectrum of G_1^{120} clearly demonstrated that each alkynyl functionality of **1** had actually reacted, with the absence of the bands assigned to propyne indicating the total removal of the leaving group during the drying step. Furthermore, above 2000 cm^{-1}, a broad absorption band due to OH stretching modes ranging from 3600 to 2500 cm^{-1} with a maximum around 3380 cm^{-1} was detected, along with weak CH stretching features at 3034 cm^{-1}. Main resonances observed below 2000 cm^{-1} included a wide band assigned to the water deformation mode, typical features of the *p*-phenylene spacer at 1478 and 1430 cm^{-1} (ν_{ring}(C=C) + ν_{ring}(C−C)), 1075 and 1011 cm^{-1} (δ(C_{ring}H in-plane)), and 798 cm^{-1} (δ(C_{ring}H out-of-plane)), and bands at 676 and 545 cm^{-1} attributed to Sn−O−Sn[36a,c] and Sn−O[36b,c] (belonging to the Sn−OH groups) stretching vibrations, respectively. Nonetheless, the peaks at 2924 and 2852 cm^{-1} (methylene stretching region) denoted the presence of traces of THF probably trapped in the xerogel. Samples G_2^{120} and G_3^{120} led to similar observations. Indeed, no evidence for any prop-1-ynyl group or propyne was detected in their FTIR spectrum. The Sn−O−Sn and Sn−O−H vibration modes were also observed in the expected wavenumber regions as well as the typical features of *p*-xylene or butylene spacers. Furthermore, according to the microanalysis data, the $Sn_2(C_6H_4)_1O_{2.5}(OH)_1(THF)_{0.2}\cdot 1.2H_2O$, $Sn_2(CH_2-C_6H_4-CH_2)_1O_{2.8}(OH)_{0.4}(THF)_{0.4}\cdot H_2O$, and $Sn_2(CH_2)_4O_{2.9}(OH)_{0.2}(THF)_{0.2}\cdot 0.2H_2O$ formulas could therefore be proposed for G_1^{120}, G_2^{120}, and G_3^{120}, respectively. As a consequence, these data were consistent with the absence of the cleavage of the Sn−C_{spacer} bond during the sol−gel process and the conservation of the molecular structure of the precursors, which gave organically bridged polystannoxanes. Furthermore, on the basis of the oxygen content determined by elemental analyses, the butylene bridge compound gave rise to more condensed, i.e., less hydroxylated, xerogels than the two other precursors, in accord with the nitrogen adsorption data (see below). These findings were in agreement with the nature of the hydrolysis products reported for trialkoxy- or trialcynylorganotins. Thus, tri(*tert*-amyloxy)- and tri(prop-1-ynyl)butyltins led to oxo-hydroxo Sn_{12} clusters bearing one hydroxyl group for six tin centers,[37] whereas tris(phenylethynyl)- and tri(prop-1-ynyl)aryltins yielded oxo-hydroxo Sn_{12} or Sn_6 clusters, including one hydroxide per tin atom.[38] Finally, attempts to determine the degree of condensation by ^{119}Sn solid-state MAS NMR studies remained unsuccessful. Two main factors might be at the origin of this behavior: the high chemical shift anisotropy magnitudes in ^{119}Sn solid-state NMR that prevent the detection of a single signal for each tin site even at high spinning rates, and the very large number of tin sites, including both crystallographic and molecular considerations, in amorphous gels, which leads to numerous poorly resolved spectra.

The solid-state properties of the xerogels were also investigated. The powder X-ray diffraction patterns demonstrated no crystallinity (Figure 3). However, in the case of G_2^{120}, a broad signal centered about $2\theta = 8°$ was observed, indicating a poorly ordered nanostructured material. This Bragg peak corresponded to a *d* spacing of about 10 nm, which was similar to the tin−tin distance deduced from the structure of **2**. These close values suggested the presence of a short-range organization induced by the *p*-xylene moieties inside the amorphous solid network. In contrast, the shorter *p*-phenylene and butylene bridges in G_1^{120} and G_3^{120} led to the absence of similar peaks in the powder X-ray diffraction patterns. Nitrogen adsorption−desorption analysis and TEM measurements revealed the formation of nonporous solids with very low specific surface areas (Table 1). Depending on the precursor nature, the specific surface areas of the xerogels indeed varied from 1.5 to 7 m^2 g^{-1}, and the total pore volumes were lower than 0.02 cm^3 g^{-1}.

Thermolytic Behavior of the Xerogels. To obtain tin dioxide materials, the hybrid xerogels had to be converted into tin dioxide by heat treatment. Annealing at a temperature too low could lead to incomplete conversion, whereas a temperature too high could bring about aggregation of the particles, which would affect the texture of the resulting material. The determination of the optimal calcination temperature was highly important for this reason as well as for energy-saving considerations. Thermogravimetry coupled to mass spectrometry (TGA−MS) studies not only provide such information but also shed light on the relative thermal stability of the hybrid xerogels prepared and the nature of the organics in the sol−gel matrices.

(36) (a) Kriegsman, H.; Hoffmann, H. M.; Geissler, H. *Z. Anal. Allg. Chem.* **1965**, *24*, 341. (b) Morrison, J. S.; Haendler, H. M. *J. Inorg. Nucl. Chem.* **1967**, *29*, 393. (c) Senguttuvan, T. D.; Malhotra, L. K. *Thin Solid Films* **1996**, *289*, 22.

(37) Ribot, F.; Banse, F.; Sanchez, C.; Tolédano, P. *Inorg. Chem.* **1995**, *34*, 6371.

(38) (a) Jaumier, P.; Jousseaume, B.; Riague, H.; Toupance, T.; Lahcini, M. In *Better Ceramics Through Chemistry: Hybrid Organic/Inorganic Materials*; Coltrain, B. K., Sanchez, C., Schaefer, D. W., Wilkes, G. L., Eds; Materials Research Society: Pittsburgh, PA, 2000; Vol. 628, p CC1.2.1. (b) Prabusankar, G.; Jousseaume, B.; Toupance, T.; Allouchi, H. *Angew. Chem., Int. Ed.* **2006**, *45*, 1255.

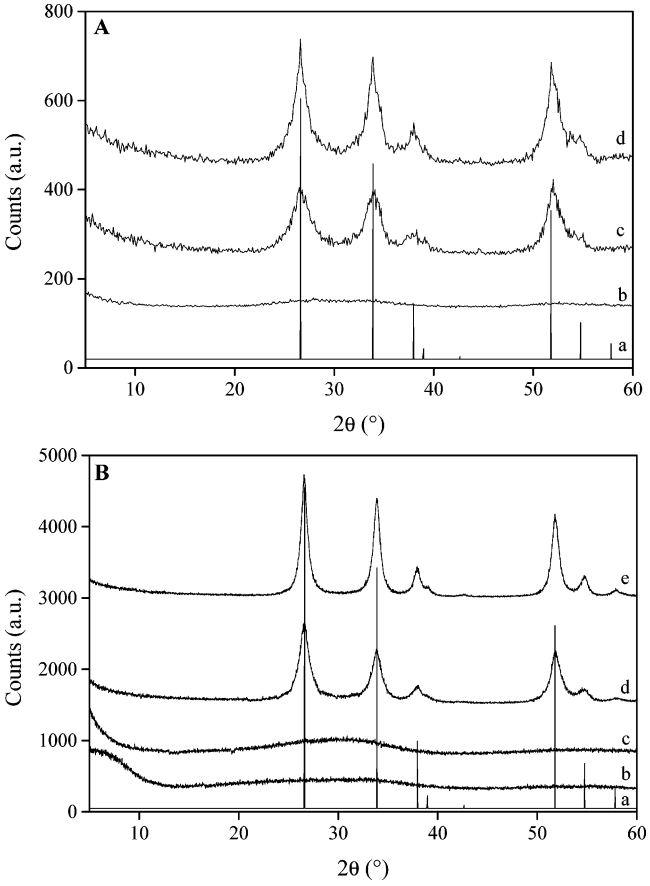

Figure 3. X-ray diffraction patterns of (A) (a) cassiterite SnO_2 (JCPDS 41-1445), (b) G_1^{120}, (c) G_1^{400}, and (d) G_1^{500} and (B) (a) cassiterite SnO_2 (JCPDS 41-1445), (b) G_2^{120}, (c) G_2^{350}, (d) G_2^{400}, and (e) G_2^{500}.

Table 1. Nitrogen Adsorption Porosimetry Studies[a] of Dried and Calcined Sol−Gel Samples

sample	S_{BET} ($m^2\ g^{-1}$)	total pore volume ($cm^3\ g^{-1}$)	mean pore diameter (nm)
G_1^{120}	7	0.02	[b]
G_1^{400}	110	0.14	5.0
G_1^{500}	70	0.12	6.5
G_2^{120}	2.5	0.01	[b]
G_2^{400}	150	0.13	<3.5
G_2^{500}	45	0.15	12
G_3^{120}	1.5	<0.01	[b]
G_3^{400}	65	0.07	4.5
G_3^{500}	40	0.08	7.5

[a] Surface areas were determined by BET, mean pore diameters by BJH theory (adsorption branch), and pore volumes by single-point analysis. [b] BJH theory cannot be used to estimate the pore size in this case.

The TG (thermogravimetric) curves depicted in Figure 4 show the change in the mass of the different xerogels between 50 and 600 °C under an air or argon flow. The TG of G_1^{120} in air showed a continuous mass loss occurring in three main successive steps of 6.4 (from 80 to 200 °C), 17.2 (from 200 to 350 °C), and 6% (from 350 to 450 °C) (for G_3^{120}: 7.6 (from 80 to 150 °C), 9.4 (from 150 to 280 °C), and 3.8% (from 280 to 550 °C)) to give a final residue of 29.6% (G_3^{120}: 20.8%). Xerogel G_2^{120} revealed a more complicated thermal decomposition pathway, with four main stages of 5.5 (from 80 to 150 °C), 3.6 (from 150 to 270 °C), 5.2 (from 270 to 350 °C), and 24.9% (from 350 to 550 °C). As a consequence, framework decomposition in air began above 180 °C for the *p*-phenylene-bridged polystannoxane and above 260 °C for the butylene- and *p*-xylene-bridged

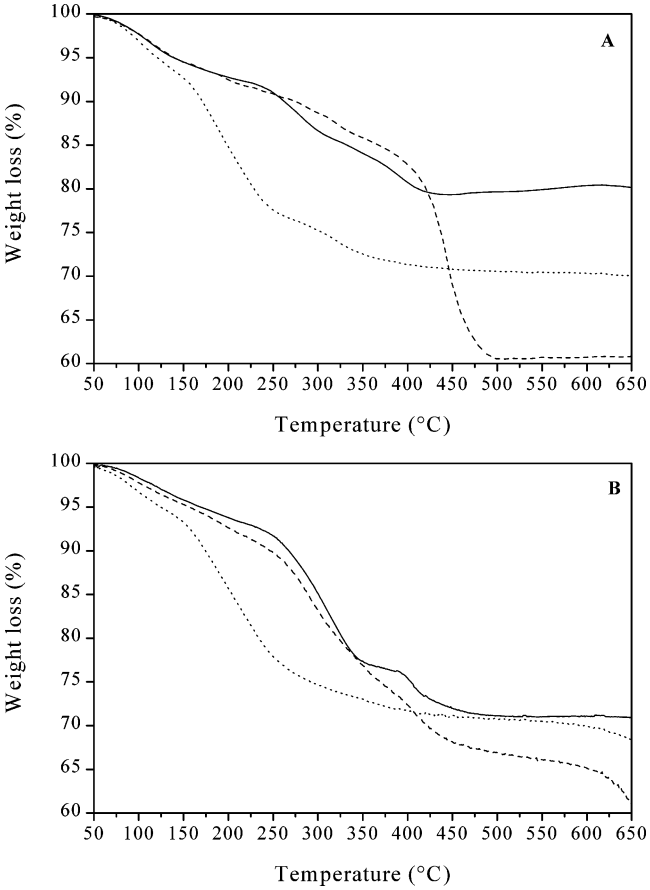

Figure 4. Thermogravimetric analysis plot of xerogels G_1^{120} (dotted line, *p*-phenylene), G_2^{120}, (dashed line, *p*-xylene), and G_3^{120} (full line, 1-butylene), under (A) air flow and (B) argon flow.

systems. However, in each case, the weight loss found was larger than the one expected for the different formula proposed for the xerogels on the basis of elemental analysis data. Incomplete combustion and oxidation of carbonaceous species might be at the origin of the differences observed.

To more closely examine the processes involved during the thermolysis, the experiments were carried out under an argon flow and the species formed were analyzed by mass spectrometry. For G_1^{120}, three mass losses, the second being the most conspicuous, were observed on the TG trace; the main molecules detected by MS measurements were water (*m*/*z* 18), carbon dioxide (*m*/*z* 22, 44), tetrahydrofurane (*m*/*z* 72), and benzene and its fragments (*m*/*z* 50, 51, 52, 76, 77, 78). According to the *m*/*z* curves as a function of temperature (Figure 5A), the different pyrolysis stages can be rationalized as follows: (i) desorption of physisorbed and chemisorbed water (from 80 to 130 °C, 5.5% mass loss); (ii) cleavage of the $Sn-C_{ar}$ bonds of the *p*-phenylene-bridged polystannoxane, yielding benzene and associated with removal of traces of solvent trapped within small pores (from 130 to 285 °C, 19.5% mass loss); (iii) loss of structural water and elimination of remaining carbon as carbon dioxide (from 285 to 425 °C, 3.1% mass loss). A similar pyrolysis pathway was found for G_3^{120}, the main differences lying in the decomposition temperature of the butylene spacer, which was found to be higher (Figure 4B, full line). In both cases, the decomposition of solvent traces overlapped with that of the organic spacer and the two contributions could not be resolved. However, the presence of *p*-phenylene and butylene bridges was clearly

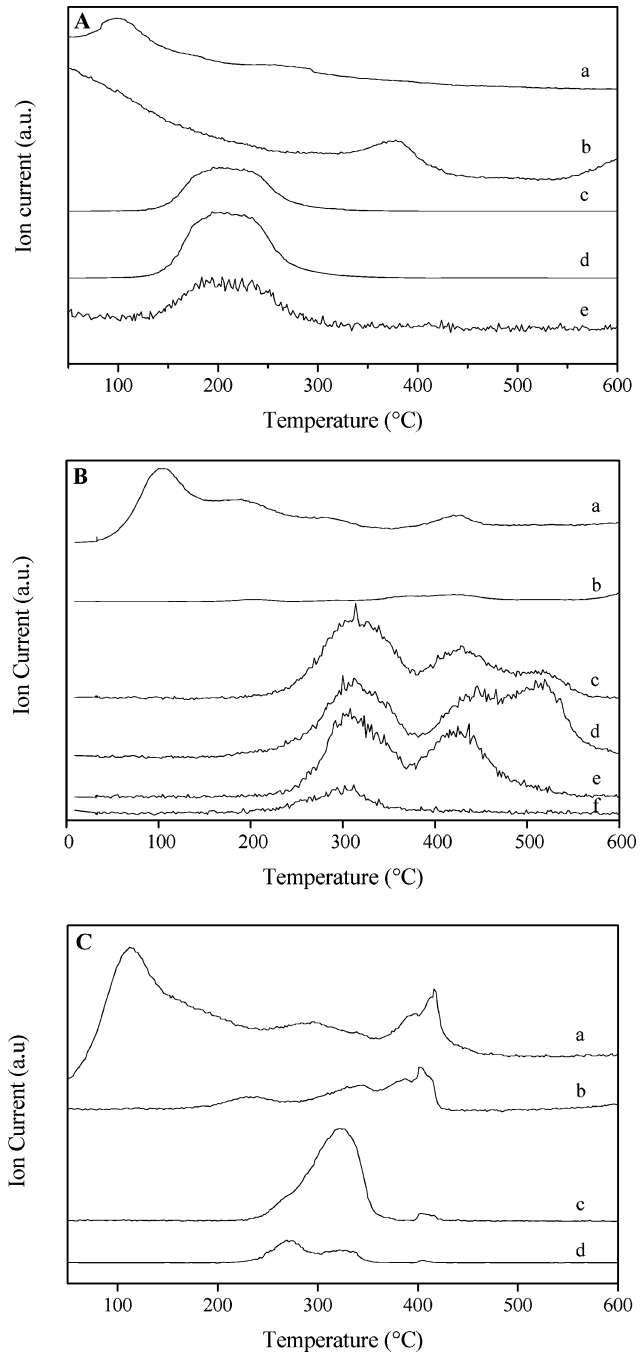

Figure 5. *m*/*z* curves as a function of temperature for (A) sample G_1^{120} (a) *m*/*z* 18 (H_2O^+), (b) *m*/*z* 44 (CO_2^+), (c) *m*/*z* 52 ($C_4H_4^+$), (d) *m*/*z* 78 ($C_6H_6^+$), and (e) *m*/*z* 72 ($C_4H_8O^+$); (B) sample G_2^{120} (a) *m*/*z* 18 (H_2O^+), (b) *m*/*z* 44 (CO_2^+), (c) *m*/*z* 52 ($C_4H_4^+$), (d) *m*/*z* 78 ($C_6H_6^+$), (e) *m*/*z* 90 ($CH_2C_6H_4^+$), (f) *m*/*z* 72 ($C_4H_8O^+$); (C) sample G_3^{120} (a) *m*/*z* 18 (H_2O^+), (b) *m*/*z* 44 (CO_2^+), (c) *m*/*z* 56 ($C_4H_8^+$), and (d) *m*/*z* 72 ($C_4H_8O^+$).

evidenced by the TGA/MS measurements. The thermolytic behavior of G_2^{120} is notably different from the previous ones. Indeed, at least four different steps could be distinguished on the TG curve (Figure 4B, dashed line), and the ion fragment versus temperature profiles of G_2^{120} could be rationalized as follows: (i) desorption of physisorbed and chemisorbed water (from 80 to 200 °C, 6% mass loss); (ii) first stage of the decomposition of the *p*-xylene spacer and release of traces of solvent trapped within small pores (from 200 to 370 °C, 19.0% mass loss); (iii) second stage of the degradation of the *p*-xylene bridge and a loss of structural water (from 370 to 470 °C, 7.5% mass loss); (iv) elimination of benzene arising from the pyrolysis of the *p*-xylene spacer (from 470 to 560 °C, 2.0% mass loss), the loss of carbon dioxide mainly occurring at temperatures higher than 650 °C (not shown). Consequently, only the decomposition products of the *p*-xylene spacer were detected, and the origin of the carbon dioxide might be related to the degradation of high-molecular-weight carbonaceous species stemming from the condensation of the organic spacer at high temperature.

To summarize, the presence of the organic spacer in the tin-based hybrid xerogels was clearly established by TGA−MS analyses and calcination temperatures higher than 400 °C were required for removing the organics.

Characterization of the Annealed Xerogels. Dried samples were treated in an oxygen flow at 400 or 500 °C for 4 h. As expected, the composition, structure, texture, and morphology of the samples underwent many changes upon annealing, with the same general trends being observed for each xerogel studied.

First of all, the resulting materials showed only bands in IR spectroscopy typical of tin oxide particles, which accounted for the complete removal of the organic spacer. For instance, below 1600 cm^{-1}, the FTIR spectra of G_1^{400} and G_1^{500} exhibited key features at ca. 680 (sh), 610, 545 (sh), and 472 cm^{-1}, falling into the range of the Sn−O stretching mode region. Consequently, two new absorptions at ca. 610 and 472 cm^{-1}, related, respectively, to the antisymmetric and symmetric Sn−O−Sn stretching modes,[39] appeared after annealing, whereas the broadband detected at ca. 540 cm^{-1} (Sn−OH stretching mode) in G_1^{120} drastically diminished (Figure 2b−d). Furthermore, the intense band at ca. 610 cm^{-1} increased in intensity and sharpened as the temperature of the heat treatment was increased. The IR data were therefore consistent with the formation of tin dioxide particles arising from the condensation of adjacent surface hydroxyl groups with the release of water.

The crystallinity of the annealed materials was then checked by powder X-ray diffraction. Prior to calcination above 400 °C, each material studied exhibited X-ray diffractograms comprising only very broad bands due to amorphous phases or very small oxide particles (graph b in part A and graphs b and c in panel B of Figure 3). In contrast, the tetragonal cassiterite tin dioxide phase was clearly identifiable in the X-ray diffraction patterns of the xerogels calcined above 400 °C, with the most intense features at *d* (Å) values of {110} (3.347), {101} (2.643), {200} (2.369), {211} (1.764), {220} (1.675), and {002} (1.593).[40] In addition, a progressive increase in peak intensity coupled with a sharpening of the peaks was observed as the temperature was increased to 500 °C, indicating an increase in crystallinity of the tin dioxide phase, probably due to the sintering process (graphs c and d in part A and graphs d and e in part B of Figure 3). The Scherer equation was employed, assuming a shape factor of 0.9, to estimate the average crystalline sizes using the SnO_2 (110) reflections.[41] Average nanocrystallite sizes of about 4 and 7.5 nm were estimated

(39) (a) Harrison, P. G.; Guest, A. *J. Chem. Soc., Faraday Trans. 1* **1987**, *83*, 3383. (b) Harrison, P. G.; Lloyd, N. C.; Daniell, W.; Bailey, C.; Azelee, W. *Chem. Mater.* **1999**, *11*, 896.
(40) JCPDS 41-1445 (cassiterite tin dioxide); International Center for Diffraction Data: Newtown Square, PA, 1998.

Table 2. Values of the Mean Crystallite Size, the Mean Particle Size and Chemical Composition

sample	mean crystallite size[a] (nm)	mean particle size[b] (nm)	C/Sn (at %)
G_1^{400}	4	10	3.9
G_1^{500}	7.5	15	2.6
G_2^{400}	7.5	12	34.9
G_2^{500}	12	25	2.5
G_3^{400}	5	12	22.7
G_3^{500}	9	17	6.3

[a] Determined from X-ray line broadening (±0.5 nm). [b] Determined from TEM images.

for G_1^{400} and G_1^{500} (Table 2), whereas the samples prepared from G_2^{120} appeared to be more crystalline, with sizes of 7.5 and 12 nm for G_2^{400} and G_2^{500}, respectively. These drastic changes were confirmed by TEM images. Thus, the large amorphous grains, without any evidence of nanopores, observed in the TEM micrographs of G_1^{120} were replaced by a network of assembled nanoparticles of various sizes and shapes after calcination (Figure 6). Not surprisingly, the SnO_2 particle sizes increased as the temperature of the thermal treatment was raised from 400 to 500 °C, which corroborated the same trends as those deduced from X-ray line broadening. Average particle sizes calculated from a large number of particles were found to be 10 and 15 nm for G_1^{400} and G_1^{500}, respectively. Furthermore, samples prepared from precursors **2** and **3** behaved similarly, even though the G_2^{400} and G_2^{500} samples were composed of more crystalline and/or larger particles.

More intricate was the influence of the thermal treatment on the textural properties of the calcined materials. Amazingly, annealing at 400 °C induced a strong enhancement of the BET surface areas, values of about 65, 110, and 150 m^2 g^{-1} were measured for G_3^{400}, G_1^{400}, and G_2^{400}, respectively. Moreover, the calcined materials prepared clearly showed a mesoporous texture, notwithstanding that samples prepared from the butylene-bridged polystannoxane G_3^{120} were less porous than the others. Thus, the N_2 adsorption isotherms of G_1^{400} and G_2^{400} exhibited a type IV-like behavior, including a type H2 hysteresis loop (Figure 7), which is typical of mesoporous materials according to the IUPAC classification.[42] For G_1^{400}, a sharp inflection of the adsorption volume at $P/P_0 = 0.45$ and a relatively steep desorption branch revealed a distribution of various sized cavities but with the same entrance diameter.[43] The pore size distribution based on the adsorption branch is quite narrow, with an average pore diameter of 5 nm. The isotherm of G_2^{400} contained features representative of smaller pores, i.e., 3.5 nm, as inferred from DFT analysis, a more valid model in this pore size range. However, a significant decrease in the specific surface areas was noted when the calcination temperature was increased to 500 °C, to reach ca. 70 m^2 g^{-1} for G_1^{500} (45 and 40 m^2 g^{-1}, respectively, for G_3^{500} and G_3^{500}). Although N_2 adsorption isotherms still showed features characteristic of mesoporous materials, the pore size distributions became much broader and the mean pore sizes increased pronouncedly. This behavior was closely related to the sintering and particle growth as mentioned above. Furthermore, the elemental analysis data provided evidence that tin dioxide was actually prepared, even though G_2^{400} still contained a rather large amount of remaining carbon. Finally, the textural properties of these materials appeared to be stable at the temperature of the thermal treatment used (i.e., 400 or 500 °C). However, both specific surface area and porous structure collapsed when the xerogels were annealed at higher temperatures.

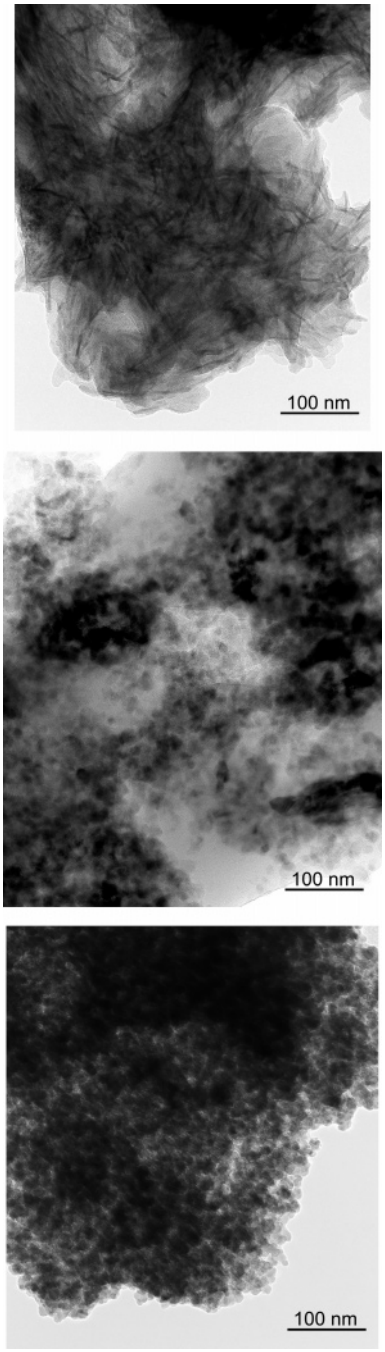

Figure 6. Transmission electron micrographs of G_1^{120} (top), G_1^{400} (middle), and G_1^{500} (bottom).

(41) The mean particle size is given by the Scherrer relation $t = (0.9\lambda)/\beta\cos(\theta)$, where λ is the wavelength, β the angular half-width of the *hkl* peak for the studied sample, and θ the Bragg angle for the chosen *hkl* reflection. See Jenkins, R.; Synder, R. L. *Introduction to X-ray Powder Diffractometry*; Wiley: New York, 1996.

(42) Sing, K. S. W.; Everett, D. H.; Haul, R. A. W.; Moscou, L.; Pierotti, R. A.; Rouquerol, J.; Siemieniewska, T. *Pure Appl. Chem.* **1985**, *57*, 603.

(43) (a) Wang, L.; Tomura, S.; Maeda, M.; Ohashi, F.; Inukai, K.; Suzuki, M. *Chem. Lett.* **2000**, *29*, 1414. (b) Yoo, K.; Choi, H.; Dionysiou, D. D. *Chem. Commun.* **2004**, 2000.

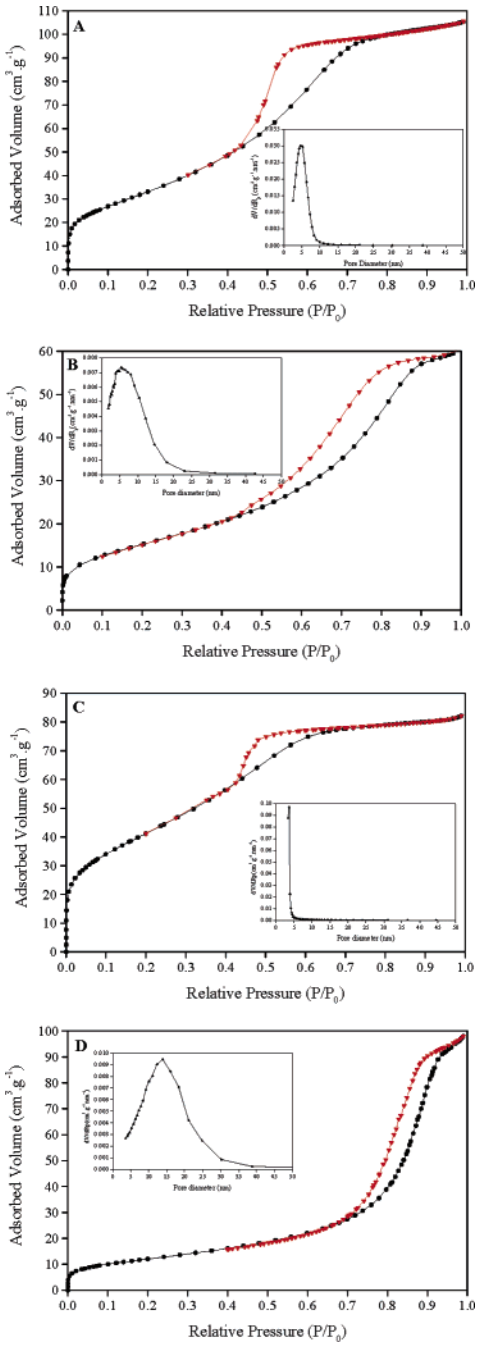

Figure 7. Nitrogen gas adsorption−desorption isotherms and pore-size distribution (inset) of (A) G_1^{400}, (B) G_1^{500}, (C) G_2^{400}, and (D) G_2^{500}.

Discussion

To the best of our knowledge, our works constitute the first preparation of transparent gels from perorganometallic compounds. Suitable organic leaving groups can therefore advantageously replace the traditional chloride or alkoxide functions usually involved in the sol−gel chemistry, which in our case presents the huge advantage of providing precursors that are easy to handle and purify. Another interest in this family of precursors is to avoid the formation of alcohol or acids, because the leaving group is removed as a gas, i.e., propyne, which prevents unwanted side reactions from taking place and the presence of undesirable organics in the xerogels. Gelling times of precursors **1**−**3**, i.e. 12−72 h, are 2 orders of magnitude longer than those reported for stabilized dialkoxytins, i.e., 0.1−0.2 h.[20c] This finding can be related to the lower reactivity of the tin−$C_{sp-hybridized}$ bond in the alkynyltins toward hydroxylated species such as water or alcohols.[31b] Furthermore, transparent gels are solely obtained when hydrolysis is conducted under acidic conditions. Indeed, acid catalysis probably favors an increase in the hydrolysis rate of the tin−alkynyl bond and a concomitant decrease in the condensation rate of the hydroxyl groups, leading to the formation of low-molecular-weight species and, as a result, to transparent media. Regardless of the bridge nature, elemental analyses, FTIR, and TGA−MS data show, without any ambiguity, that the Sn−C_{spacer} bonds are maintained in the xerogels and that the organic units are structural components of the framework. Generally speaking, the materials obtained are amorphous and nonporous. The texture (specific surface area and porosity) of these hybrids is poorer than that reported for most of the materials prepared from silicon analogues under similar experimental conditions.[44] Tin-based hybrid xerogels therefore appear to be more condensed than their silicon counterparts, in which the large number of unreacted silanol groups inhibits the network from becoming denser. However, slight textural differences can be noticed between the prepared tin-based hybrids. A slightly higher specific surface area is indeed found with the rigid electron-withdrawing *p*-phenylene spacer, whereas the flexible electron-donating butylene bridge, which allows the network to condense more readily, leads to the lowest specific surface area. Moreover, on the basis of the XRD data, preferential alignment of the organic bridge starts to occur as the longer rigid *p*-xylene spacer is utilized, a general tendency that was clearly confirmed by the self-assembly process observed for tin-based hybrid materials including long rigid spacers.[33] All these data are therefore consistent with the formation of kinetically controlled xerogels as previously proposed in the case of organically bridged hybrid silicas.[44] Nonetheless, the main influence observed with the nature of the organic bridge concerns the thermal stability of the xerogels and the textural properties of the materials obtained after calcination.

At first, the hybrid materials display relative thermal stabilities in the order butylene = *p*-xylene > *p*-phenylene, which is very different from the behavior of the corresponding bridged silsesquioxanes.[28] This stability order cannot be explained in a straightforward manner. Thus, it does not follow the one expected from the cleavage ability of tin−carbon bonds toward ionic or radical reagents, which increases in the order Sn−CH_2CH_3 < Sn−Ph < Sn−CH_2-Ph. Similarly, no obvious correlation can be drawn with the bond dissociation enthalpies, which decrease in the order Sn−Ph > Sn−CH_2CH_3 > Sn−CH_2Ph.[45] As a result, the order observed likely results from different antagonistic contributions leading to an easier departure of the *p*-phenylene spacer under the thermolytic conditions used.

More interestingly, the texture and the morphology of samples calcined at a given temperature strongly depend on the starting xerogel. In each case, the detection of structural water by TGA/MS provides evidence that condensation of

(44) Cerveau, G.; Corriu, R. J. P.; Framery, E. *Chem. Mater.* **2001**, *13*, 3373.
(45) Davies, A. G. *Organotin Chemistry*; Wiley-VCH: Weinheim, Germany, 2004; p 27.

neighboring surface hydroxyl groups occurs, creating new tin−oxygen−tin bridges via oxolation reactions

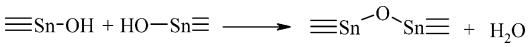

These reactions are activated by various processes as the network shrinkage induced by the annealing and the steric hindrance decrease around the tin centers because of the pyrolysis of the organic spacers. At different stages of the thermal treatment, both processes may force the close matching of reactive hydroxyl groups, leading to a continuous water emission. This is well-known to cause a severe drop in the specific surface area by closure of the porosity and/or particle growth. However, the formation of pores arising from the decomposition of the organic spacer clearly competes with this process in the present work. As a matter of fact, annealing not only enables the elimination of the organics from the xerogels with the concomitant formation of tin dioxide particles but also significantly improves the textural properties of the resulting materials. Regardless of the organic bridge, the specific surface areas increase by more than 1 order of magnitude after annealing at 400 °C, with BET surface areas as high as 110−150 m^2 g^{-1} being reached in the case of the materials synthesized from G_1^{120} and G_2^{120}. Although the size of the pores is larger than the length of the organic spacer removed during the calcination step, the pore-size distribution remains narrow, with mean pore sizes of 3.5−5 nm. In contrast, the more condensed xerogel G_3^{120} gives significantly lower surface areas and larger pore sizes from calcination at 400 °C. As the temperature of the thermal treatment is increased to 500 °C, the condensation process described above prevails and the textural properties are spoiled in all cases.

Organically bridged ditin hexaalkynides **1**−**3** are therefore relevant sol−gel precursors of mesoporous (or nanoporous) tin dioxide materials. The porosity evidenced by N_2 adsorption measurements for annealed samples clearly falls into the mesoporous range according to the UIPAC classification (pore diameters between 2 and 50 nm).[42] On the basis of the TEM images and XRD patterns, the annealed materials consist of a porous network of aggregated cassiterite tin dioxide nanoparticles, the mesoporosity detected stemming from the interparticle space. Nevertheless, the particle sizes estimated from TEM photographs are larger than the crystallite sizes deduced from X-ray diffractograms. This may be rationalized by considering that the Scherer formula can lead to an underestimation of the average crystallite size because the contribution of smaller size components in a crystallite-size distribution dominates the line broadening in the XRD patterns. As a consequence, the actual crystallite size might be larger than that estimated by XRD measurements and be closer to the average particle size determined from the TEM micrographs.

Bis(triprop-1-ynylstannyl)benzene **1** appears to be the most relevant precursor of nanocrystalline mesoporous SnO_2 for application purposes. In comparison with **2** and **3**, compound **1** yields pure cassiterite tin dioxide materials with very low carbon amounts from calcination at 400 °C because of the prompt removal of the *p*-phenylene spacer. After annealing at 400 and 500 °C, the BET surface area (110 and 70 m^2 g^{-1}), the mean pore size diameter (5 and 6.5 nm), and the mean crystallite size (4.5 and 7 nm) are similar to those reported for tin dioxide materials prepared by the template method after treatment in the same temperature range.[4b,27e] Moreover, the specific surfaces areas are large, because they are equivalent to 300 and 190 m^2 g^{-1} for siliceous materials after normalization to account for the difference in density between silica and tin dioxide. These materials may therefore be used as the active layer for applications requiring high surface area, porosity, and crystallinity. In particular, they could be advantageously used to detect gases, such as hydrogen or nitrogen oxides, for which the working sensor temperature is below 300 °C.[46] Last, it is worthwhile to mention that precursor **2** leads to more crystalline tin oxide powders than **1** with close textural properties, but with larger carbon contents. The remaining polluting carbon therefore constitutes a great inconvenience for most of the applications, but it might be exploited in lithium-ion batteries wherein tin oxide is used as anode materials in the presence of carbon black or graphite.[47]

Conclusion

Acidic hydrolysis of organically bridged ditin hexaalkynides **1**−**3** followed by annealing at 400−500 °C for several hours gave nanocrystalline nanoporous tin dioxide materials. Depending on the precursor nature and the calcination conditions, the preparation of materials with surface areas ranging from 40 to 150 m^2 g^{-1}, an average pore size between 3.5 and 12 nm, and a mean particle size ranging from 5 to 25 nm was achieved. In each case, a porous network of aggregated nanoparticles was prepared, with the nanoporosity corresponding to the interparticle space. The best strategy for obtaining pure nanocrystalline tin dioxide materials with good textural properties is to start from **1**, whose *p*-phenylene bridge is easily removed by calcination. This achievement represents a first step toward the preparation of nanocrystalline nanoporous tin dioxide thin films for gas sensing or solar-light energy conversion purposes. Our group is currently developing efforts in this direction and the findings will be presented very soon.

Acknowledgment. The authors thank the Aquitaine Region, the Centre National de la Recherche Scientifique (Material Program Grant), and the European Community (FAME Network of Excellence) for partial financial support of this work.

CM061964D

(46) (a) Zhang, G.; Liu, M. *Sens. Actuators, B* **2000**, *69*, 144. (b) Hyodo, T.; Sasahara, K.; Shimizu, Y.; Egashira, M. *Sens. Actuators, B* **2000**, *106*, 580.

(47) (a) Aurbach, D.; Nimberger, A.; Markovsky, B.; Levi, E.; Sominski, E.; Gedanken, A. *Chem. Mater.* **2005**, *14*, 4155. (b) Wang, Y.; Lee, J. Y.; Zheng, H. C. *Chem. Mater.* **2005**, *17*, 3899.